Article

Fine-regolith production on asteroids controlled by rock porosity

https://doi.org/10.1038/s41586-021-03816-5

Received: 11 March 2021

Accepted: 8 July 2021

Published online: 6 October 2021

Check for updates

S. Cambioni[1,2✉], M. Delbo[3], G. Poggiali[4], C. Avdellidou[3], A. J. Ryan[1], J. D. P. Deshapriya[5], E. Asphaug[1], R.-L. Ballouz[1], M. A. Barucci[5], C. A. Bennett[1], W. F. Bottke[6], J. R. Brucato[4], K. N. Burke[1], E. Cloutis[7], D. N. DellaGiustina[1], J. P. Emery[8], B. Rozitis[9], K. J. Walsh[6] & D. S. Lauretta[1]

Spacecraft missions have observed regolith blankets of unconsolidated subcentimetre particles on stony asteroids[1–3]. Telescopic data have suggested the presence of regolith blankets also on carbonaceous asteroids, including (101955) Bennu[4] and (162173) Ryugu[5]. However, despite observations of processes that are capable of comminuting boulders into unconsolidated materials, such as meteoroid bombardment[6,7] and thermal cracking[8], Bennu and Ryugu lack extensive areas covered in subcentimetre particles[7,9]. Here we report an inverse correlation between the local abundance of subcentimetre particles and the porosity of rocks on Bennu. We interpret this finding to mean that accumulation of unconsolidated subcentimetre particles is frustrated where the rocks are highly porous, which appears to be most of the surface[10]. The highly porous rocks are compressed rather than fragmented by meteoroid impacts, consistent with laboratory experiments[11,12], and thermal cracking proceeds more slowly than in denser rocks. We infer that regolith blankets are uncommon on carbonaceous asteroids, which are the most numerous type of asteroid[13]. By contrast, these terrains should be common on stony asteroids, which have less porous rocks and are the second-most populous group by composition[13]. The higher porosity of carbonaceous asteroid materials may have aided in their compaction and cementation to form breccias, which dominate the carbonaceous chondrite meteorites[14].

Between April and June 2019, the Origins, Spectral Interpretation, Resource Identification, and Security Regolith Explorer (OSIRIS-REx) Thermal Emission Spectrometer[15] (OTES) measured thermal infrared emission spectra from the surface of Bennu at different local times of day. These spectra are a function of surface temperature, which varies throughout the day and night depending on surface roughness θ and thermal inertia Γ. The roughness is due to surface irregularities that are not resolved in global topography but still affect temperatures because of shadows and self-heating[16]. The thermal inertia measures the resistance of the materials to temperature change; it is determined from the thermal conductivity κ, heat capacity c_P and bulk density ρ as $\Gamma = (\kappa c_P \rho)^{1/2}$, and allows us to distinguish different geological units, such as fine regolith and rocks.

Here, fine regolith means unconsolidated particles smaller than the e-folding depth of the diurnal thermal wave (l_s; a few centimetres on Bennu[10]), whereas rocks are defined as any surface material of size $D_R > l_s$. The thermal inertia of fine regolith (Γ_P) is lower than that of rocks of same composition (Γ_R) because radiative thermal conduction between particles is less efficient than phononic heat transfer in an individual particle or rock[16]. Thus, fine regolith is hotter than rocks during the day, and vice versa during the night. Fine regolith and rocks contribute to the infrared emission proportionally to their surface abundances, α and $(1-\alpha)$, respectively[17].

To distinguish fine regolith from rocks on Bennu, we use a machine learning method[17] that explores all possible combinations of the spectral signals of fine regolith and rocks as a function of their surface abundance, roughness and respective thermal inertia until the OTES daytime and night-time observations are simultaneously fitted (Methods). We use our method to derive Γ_P, Γ_R and α in 122 quasi-randomly distributed OTES footprints (spots) of about 40 m in diameter (Supplementary Table 1, Extended Data Fig. 1). These spots include the two best-observed areas on Bennu: the designated backup and primary sampling sites of OSIRIS-REx, called Osprey and Nightingale, respectively.

We find that α varies between a few and several tens of per cent (Fig. 1) and that there is less fine regolith at Osprey than at Nightingale, consistent with the surface abundance of unresolved materials seen in OSIRIS-REx PolyCam images (Extended Data Fig. 2). The values of α are also consistent with the surface abundance of unresolved materials in PolyCam images at coarser spatial resolution (Methods, Extended Data Fig. 3). The measured Γ_R encompasses a continuum of values between

[1]Lunar and Planetary Laboratory, University of Arizona, Tucson, AZ, USA. [2]Division of Geological and Planetary Sciences, California Institute of Technology, Pasadena, CA, USA. [3]Université Côte d'Azur, Observatoire de la Côte d'Azur, CNRS, Laboratoire Lagrange, Nice, France. [4]INAF – Osservatorio Astrofisico di Arcetri, Florence, Italy. [5]LESIA, Observatoire de Paris, Université PSL, CNRS, Sorbonne Université, Univ. Paris Diderot, Sorbonne Paris Cité, Meudon, France. [6]Southwest Research Institute, Boulder, CO, USA. [7]Department of Geography, University of Winnipeg, Winnipeg, Manitoba, Canada. [8]Department of Astronomy and Planetary Science, Northern Arizona University, Flagstaff, AZ, USA. [9]School of Physical Sciences, The Open University, Milton Keynes, UK. ✉e-mail: saveriocambioni@email.arizona.edu

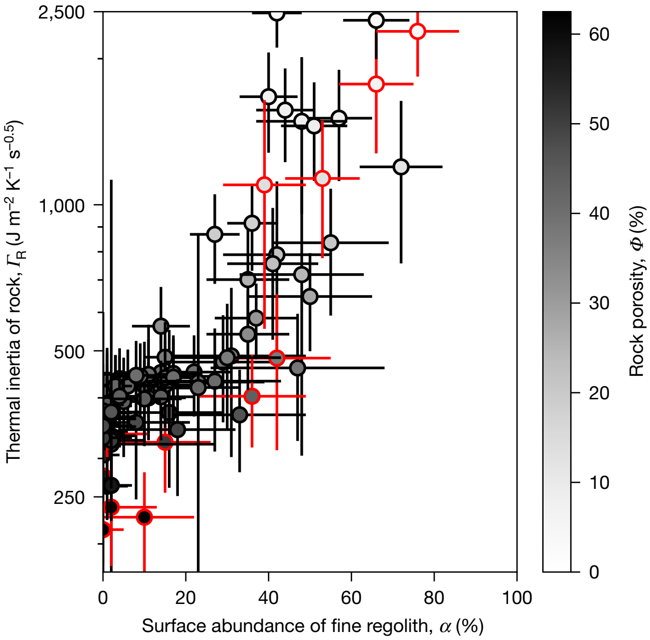

Fig. 1 | The thermal inertia of Bennu's rocks is positively correlated with the local surface abundance of fine regolith. The grey shading of the data corresponds to the porosity Φ estimated from Γ_R (Methods). The red points correspond to 13 areas where α could be overestimated because of the presence[10] of boulders for which Γ_R could be lower than the threshold value between fine regolith and rocks (Methods). The plotted data have a goodness of fit of $\chi_r^2 < 3$ (Methods), which is satisfactory for these types of observation. The error bars correspond to one standard deviation (Supplementary Table 1, Methods), computed from about 670 samples on average.

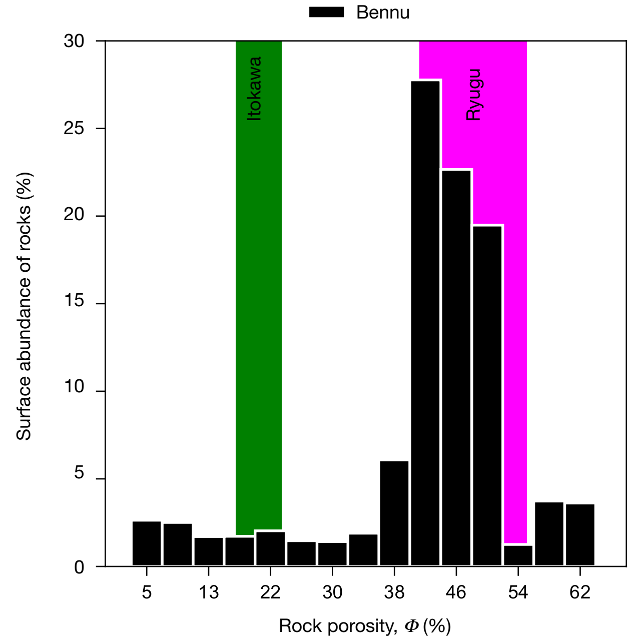

Fig. 2 | The porosities of most of Bennu's and Ryugu's rocks are much higher than that of Itokawa's rocks. The porosities of Bennu's rocks are weighted according to rock abundance (1 − α) and binned using the Freedman–Diaconis rule. The magenta and green shaded areas indicate the estimated surface-averaged ranges of rock porosity on Ryugu[18,19] and Itokawa[17], respectively. About 70% of the rocks on Bennu are as porous as those on Ryugu, whereas only about 5% of Bennu's rocks have porosity similar to that of Itokawa's rocks.

about 250 J m^{-2} K^{-1} s$^{-0.5}$, close to that derived[18,19] for Ryugu's boulders, and more than 1,000 J m^{-2} K^{-1} s$^{-0.5}$, close to that of CM2 carbonaceous chondrites[20] with compositions analogous to that spectroscopically inferred for Bennu[21]. For $\alpha \approx 0$, Γ_R is within the range of thermal inertia values derived in a previous study[10], which assumes that the surface in the OTES spot is composed of a single geological unit.

We observe a direct correlation between Γ_R and α (Fig. 1), with a Spearman correlation coefficient of $R = 0.56 \pm 0.06$ and a probability of non-correlation of $P < 4 \times 10^{-3}$ (Methods, Extended Data Fig. 4). The correlation is robust ($R = 0.54 \pm 0.07$; $P < 0.05$) when we reject spots where the thermophysical model may confuse very low-Γ_R boulders as fine-regolith-covered areas (Methods, Fig. 1). The correlation is also robust against the choice of a model parameter that represents the macroporosity of the fine regolith (Methods, Extended Data Fig. 5). In addition, we demonstrate that the correlation is not an artefact of thermophysical modelling (Methods, Extended Data Fig. 6). Finally, we do not see an inverse correlation between α and the size of the largest boulders in the OTES spots (Methods, Extended Data Fig. 7), thus ruling out the possibility that the Γ_R–α correlation is due to the sizes of the boulders (larger boulders may have lower Γ_R than smaller ones[10]).

Because fine regolith is more abundant where rocks have higher Γ_R (Fig. 1), and because Γ_R is a monotonically decreasing[19] function of rock porosity (Methods), we deduce that the surface abundance of fine regolith is lower where the nearby rocks are more porous (Fig. 1). We argue that the correlation of Fig. 1 may be explained by the dependence of regolith-forming processes (collisional and thermal fragmentation of rocks) on rock porosity.

Collisional fragmentation is driven by meteoroid impacts, craters from which have been observed[6] on rocks with $D_R \gg l_s$. Craters on rough-textured rocks were measured, using the OSIRIS-REx Laser Altimeter, to have a higher depth-to-diameter ratio than those on smoother rocks[6]. Because the depth-to-diameter ratio of craters typically increases with increasing target porosity[11,22], we deduce that Bennu hosts rocks of different porosities, consistent with Fig. 1 and ref. [10] but independently of OTES data. Impact experiments show that: (1) a lower-porosity rock requires a lower energy per unit mass to be broken than a higher-porosity rock, because in the latter impact energy is spent on pore-space collapse[11] and compaction[12] during initial crater formation; (2) the mass of crater ejecta, which could partially contribute to fine regolith, decreases with increasing target porosity[11]; and (3) craters formed on low-porosity ($\Phi \approx 25\%$) rock simulants of Bennu's composition have spalls[23], which increase fragment production. Conversely, spalling was rarely observed around craters on Bennu's rocks[6]. We deduce that collisional fragmentation increases with decreasing rock porosity and is frustrated on Bennu's rocks, which typically have $\Phi > 25\%$ (Fig. 2).

Rocks on asteroids may develop fatigue fractures to release the mechanical stresses generated by diurnal temperature cycling[24]. It is postulated that these fractures grow until breaking the host rocks, thereby producing regolith[24]. Exfoliation fractures with sizes between a few centimetres and few metres have been observed[8] on Bennu, consistent with the aforementioned process. To investigate regolith formation by thermal fatigue, we model (Methods) the time to break two rocks on Bennu that have porosities of $\Phi = 20\%$ and $\Phi = 40\%$. We find that the break-up time is shorter for the rock with $\Phi = 20\%$ than for that with $\Phi = 40\%$ (Extended Data Fig. 8), suggesting that fine regolith is more likely to be produced from the former. This is consistent with the correlation in Fig. 1.

We infer that low-porosity rocks produce more fine regolith than do high-porosity rocks, both from meteoroid impacts and from thermal cracking (Fig. 3). This explains the lack of extensive fine-regolith-covered areas on Bennu[9], where most rocks are highly porous[10] (Fig. 2). We argue that the frustration of fine-regolith build-up in the presence of high-porosity rocks could be a general phenomenon on asteroids.

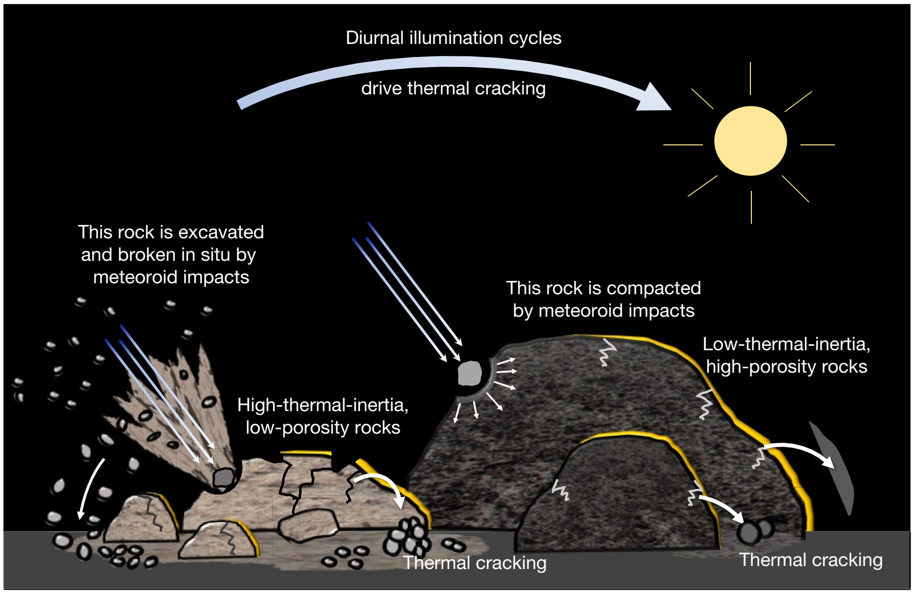

Fig. 3 | Fine-regolith production is frustrated in the presence of high-porosity rocks. On asteroids, rocks with higher porosity are compacted by meteoroid impacts rather than excavated[12]. Thermal stresses in a more porous rock are weaker in magnitude than in a denser rock[8], which means that the former could be less prone to producing fine regolith than is the latter.

Analysis of thermal images acquired by JAXA's Hayabusa2 mission[18,25] indicates that Ryugu's surface globally has $\Gamma \approx 225 \pm 45\,\mathrm{J\,m^{-2}\,K^{-1}\,s^{-0.5}}$, that some boulders with $D_R > 50$ m have $\Gamma_R \approx 115$–$160\,\mathrm{J\,m^{-2}\,K^{-1}\,s^{-0.5}}$ and that a few small boulders have $\Gamma_R \approx 600$–$1{,}000\,\mathrm{J\,m^{-2}\,K^{-1}\,s^{-0.5}}$, suggesting that most rocks on Ryugu have porosities similar to those on Bennu ($\Phi \approx 40\%$–50%) (Fig. 2, Methods). For $\Phi \approx 40\%$–50%, the correlation in Fig. 1 indicates that Ryugu, like Bennu, should have less fine regolith on the surface than do asteroids with lower-porosity rocks.

Conversely, disk-integrated infrared measurements of the stony asteroid (25143) Itokawa have revealed[17] that its rocks have $\Gamma_R \approx 900\,\mathrm{J\,m^{-2}\,K^{-1}\,s^{-0.5}}$, corresponding to $\Phi = 20\% \pm 4\%$ (Methods), which is lower than that for most rocks on Bennu and Ryugu (Fig. 2). Hence, the correlation in Fig. 1 implies that Itokawa's most common rocks produce more fine regolith than do Bennu's and Ryugu's. Spacecraft images show that Itokawa's geopotential lows are smooth terrains covered in centimetre-sized regolith[2], whereas Bennu's and Ryugu's are not[7,9]. Itokawa's smooth terrains may have formed via global particle-size sorting induced by surface mass motion[2]. Signatures of mass motion were also observed on Bennu[26] and Ryugu[7], but smooth fine-regolith-covered terrains are lacking[7,9], suggesting that Bennu's and Ryugu's surface abundances of fine regolith may be globally lower than Itokawa's. This is consistent with our analysis.

On small asteroids, fine regolith could be emplaced far from the source rock via electrostatic lofting[27], ejection during thermal exfoliation[8] and/or meteoroid impacts[22]. However, the robustness of the Γ_R–α correlation rules out an isotropically fine-regolith redistribution from each local source on Bennu. Further, electrostatic lofting is inefficient at mobilizing centimetre-sized particles[27], exfoliation is only one aspect of thermal cracking (the other being rock breakup by through-going fracturing without fragment ejection), and the current understanding[22] is that little mass should be retained by small asteroids from crater ejecta produced by impacts on low-porosity rocks. However, rocks broken in tightly clustered pieces have been observed on Bennu[8,9,28] (Extended Data Fig. 9), suggesting that regolith is produced by in situ fragmentation of large rocks exposed on the surface, similarly to what has been observed on the Moon[29]. Finally, Itokawa may lose more crater ejecta to space than do Bennu and Ryugu because average ejection velocities decrease with increasing target porosity[22]. Despite this, smooth terrains were observed only on Itokawa[2,7,9]. This suggests that Itokawa's fine-regolith losses are compensated by a higher fine-regolith production than are Bennu's and Ryugu's.

The wide range of rock porosities measured on Bennu and Ryugu probably originated on their parent bodies[25]. We postulate that high-porosity rocks subjected to impacts may be compacted without target disruption[30]. Crushing in high-porosity materials may enhance shear strain and cause associated frictional heating[31]; this may have assisted lithification of the chondrite precursors into the lower-porosity carbonaceous breccias that dominate the CM and CI meteorite collection[14] and were also observed on Bennu[28] and Ryugu[7].

Online content

Any methods, additional references, Nature Research reporting summaries, source data, extended data, supplementary information, acknowledgements, peer review information; details of author contributions and competing interests; and statements of data and code availability are available at https://doi.org/10.1038/s41586-021-03816-5.

1. Veverka, J. et al. The landing of the NEAR-Shoemaker spacecraft on asteroid 433 Eros. *Nature* **413**, 390–393 (2001).
2. Miyamoto, H. et al. Regolith migration and sorting on asteroid Itokawa. *Science* **316**, 1011–1014 (2007).
3. Huang, J. et al. The Ginger-shaped Asteroid 4179 Toutatis: new observations from a Successful Flyby of Chang'e-2. *Sci. Rep.* **3**, 3411 (2013).
4. Emery, J. et al. Thermal infrared observations and thermophysical characterization of OSIRIS-REx target asteroid (101955) Bennu. *Icarus* **234**, 17–35 (2014).
5. Müller, T. et al. Hayabusa-2 mission target asteroid 162173 Ryugu (1999 JU3): searching for the object's spin-axis orientation. *Astron. Astrophys.* **599**, A103 (2017).
6. Ballouz, R.-L. et al. Bennu's near-Earth lifetime of 1.75 million years inferred from craters on its boulders. *Nature* **587**, 205–209 (2020).
7. Sugita, S. et al. The geomorphology, color, and thermal properties of Ryugu: implications for parent-body processes. *Science* **364**, eaaw0422 (2019).
8. Molaro, J. L. et al. Thermal fatigue as a driving mechanism for activity on asteroid Bennu. *J. Geophys. Re. Planets* **125**, e2019JE006325 (2020).
9. Lauretta, D. et al. The unexpected surface of asteroid (101955) Bennu. *Nature* **568**, 55–60 (2019).
10. Rozitis, B. et al. Asteroid (101955) Bennu's weak boulders and thermally anomalous equator. *Sci. Adv.* **6**, eabc3699 (2020).
11. Flynn, G. J. et al. Hypervelocity cratering and disruption of porous pumice targets: implications for crater production, catastrophic disruption, and momentum transfer on porous asteroids. *Planet. Space Sci.* **107**, 64–76 (2015).

12. Housen, K. R., Sweet, W. J. & Holsapple, K. A. Impacts into porous asteroids. *Icarus* **300**, 72–96 (2018).
13. DeMeo, F., Alexander, C., Walsh, K., Chapman, C. & Binzel, R. in *Asteroids* Vol. IV (eds) 13–41 (2015).
14. Bischoff, A., Scott, E. R. D., Metzler, K. & Goodrich, C. A. in *Meteorites and the Early Solar System* vol. II (eds) 679 (2006).
15. Christensen, P. R. et al. The OSIRIS-REx thermal emission spectrometer (OTES) instrument. *Space Sci. Rev.* **214**, 87 (2018).
16. Delbo, M., Mueller, M., Emery, J. P., Rozitis, B. & Capria, M. T. in *Asteroids* Vol. IV (eds) 107–128 (2015).
17. Cambioni, S., Delbo, M., Ryan, A. J., Furfaro, R. & Asphaug, E. Constraining the thermal properties of planetary surfaces using machine learning: application to airless bodies. *Icarus* **325**, 16–30 (2019).
18. Shimaki, Y. et al. Thermophysical properties of the surface of asteroid 162173 Ryugu: infrared observations and thermal inertia mapping. *Icarus* **348**, 113835 (2020).
19. Grott, M. et al. Low thermal conductivity boulder with high porosity identified on C-type asteroid (162173) Ryugu. *Nat. Astron.* **3**, 971–976 (2019).
20. Opeil, C. P., Britt, D. T., Macke, R. J. & Consolmagno, G. J. The surprising thermal properties of CM carbonaceous chondrites. *Meteorit. Planet. Sci.* **55**, E1–E20 (2020).
21. Hamilton, V. et al. Evidence for widespread hydrated minerals on asteroid (101955) Bennu. *Nat. Astron.* **3**, 332–340 (2019).
22. Michikami, T., Moriguchi, K., Hasegawa, S. & Fujiwara, A. Ejecta velocity distribution for impact cratering experiments on porous and low strength targets. *Planet. Space Sci.* **55**, 70–88 (2007).
23. Avdellidou, C. et al. Very weak carbonaceous asteroid simulants I: mechanical properties and response to hypervelocity impacts. *Icarus* **341**, 113648 (2020).
24. Delbo, M. et al. Thermal fatigue as the origin of regolith on small asteroids. *Nature* **508**, 233–236 (2014).
25. Okada, T. et al. Highly porous nature of a primitive asteroid revealed by thermal imaging. *Nature* **579**, 518–522 (2020).
26. Jawin, E. et al. Global patterns of recent mass movement on asteroid (101955) Bennu. *J. Geophys. Res. Planets* **125**, e2020JE006475 (2020).
27. Hsu, H., Wang, X., Carroll, A., Hood, N. & Horanyi, M. Electrostatic removal of fine-grained regolith on sub-km asteroids. In *AAS/Division for Planetary Sciences Meeting Abstracts* Vol. 52, 402.06 (2020).
28. Walsh, K. et al. Craters, boulders and regolith of (101955) Bennu indicative of an old and dynamic surface. *Nat. Geosci.* **12**, 242–246 (2019).
29. Ruesch, O. et al. In situ fragmentation of lunar blocks and implications for impacts and solar-induced thermal stresses. *Icarus* **336**, 113431 (2020).
30. Scott, E. R. D. & Bottke, W. F. Impact histories of angrites, eucrites, and their parent bodies. *Meteorit. Planet. Sci.* **46**, 1878–1887 (2011).
31. Bland, P. A. et al. Pressure-temperature evolution of primordial solar system solids during impact-induced compaction. *Nat. Commun.* **5**, 5451 (2014).

Publisher's note Springer Nature remains neutral with regard to jurisdictional claims in published maps and institutional affiliations.

Methods

Two-component thermophysical modelling

The global mosaic of images[32] acquired by the PolyCam imager of the OSIRIS-REx Camera Suite (OCAMS[33]) with resolution of 5 cm per pixel shows that Bennu's surface is composed of a mixture of rocks and, to a lesser extent, unresolved materials[28,34]. The latter may include fine regolith with particle size $D_{\mathrm{P}} < l_{\mathrm{s}} = [\kappa/(c_{\mathrm{P}}\rho)p/\pi]^{1/2}$, where p is the rotation period of the asteroid. These observations motivate us to determine the surface abundance of fine regolith (α) with respect to the surface abundance ($1-\alpha$) of rocks with $D_{\mathrm{R}} > l_{\mathrm{s}}$.

To this end, we select 122 quasi-randomly distributed regions (OTES spots) (Extended Data Fig. 1) and use a machine learning two-component thermophysical model[17] to simultaneously fit infrared radiance spectra emitted from the asteroid at the local times of 3:20 am and 3:00 pm to derive the surface properties ($\theta, \Gamma_{\mathrm{P}}, \Gamma_{\mathrm{R}}, \alpha$). The 3:20 am station is the coldest and farthest in time from sunrise, when the brightness temperature of smaller rocks may approach that of colder fine regolith; the 3:00 pm station is diametrically opposed to the 3:20 am station, close to the time of peak surface temperature, and not at the crossing point between diurnal temperature curves for different Γ, where the thermophysical solution could be degenerate (figure 2 in ref. [10]). Furthermore, the spots on the surface for the 3:00 pm and 3:20 am stations are well aligned, which minimizes mismodelling. Modelling 122 areas instead of the full surface makes the machine learning analysis computationally feasible while still investigating a representative sample of Bennu's surface. Of the 122 spots, 100 were randomly selected and 22 were manually added to be centred as much as possible on distinct, interesting and representative geological features such as the designated sampling sites, large boulders filling the OTES spot, regions with high boulder abundance and areas with low boulder abundance.

For each area and time of day, we use the OTES' acquisition mid-observation time and boresight to calculate the longitude and latitude of the OTES spot's centre and diameter projected on Bennu's surface. The surface is modelled using the 6-m-resolution SPC/OLA v34 shape model composed of triangular facets and derived from a combination of stereophotoclinometry and laser ranging[35]; its pole orientation[9,10] is J2000 ecliptic longitude 69.92° and latitude −83.45°. The observation geometry for each spot and time of day (that is, ephemerides of the OSIRIS-REx spacecraft and the asteroid) is computed using the spiceypy Python wrapper for the SPICE toolkit. The kernel files are sourced directly from the SPICE kernels produced by the mission. For each observation geometry, we build the local set of facets of Bennu's topographic model by drawing concentric circles (with radius ranging between 0 and that of the OTES spot and centred at the spot's centre) and by drawing radial vectors with origin in the spot's centre and length between 0 and the spot's radius. Because we limited our survey to latitudes between ±60°, each OTES spot is well approximated by a circle with a diameter of 40 m that corresponds to the instrument footprint. All the unique facets that lie at the intersection between a circle and a radial vector belong to the local set.

For each OTES spot and for each observation time, we set up thermophysical simulations using a well defined model[16] that uses the aforementioned observation geometry, asteroid illumination, asteroid spin state and local sets of facets of Bennu's shape model as input. We create lookup tables of simulations where Γ varies between 25 J m^{-2} K^{-1} s$^{-0.5}$ and 2,500 J m^{-2} K^{-1} s$^{-0.5}$ (the upper limit corresponds to low-porosity meteorites[20]) in steps of 25 J m^{-2} K^{-1} s$^{-0.5}$ and θ is modelled using hemispherical craters with the surface crater density f_{c} ranging between 0 and 0.99 in steps of 0.14 (as such, $\theta = 49 f_{\mathrm{c}}^{1/2}$ represents roughness root-mean-square slope[10]). We assume a fixed value of bolometric Bond's albedo equal to 0.02 and infrared emissivity $\varepsilon = 0.95$ (as done previously[10]). The shape model's rotation and daily temperature cycle are simulated for 15 Julian days until the temperature cycle converges to a stable cycle. After this, we output the simulated radiance at the epoch of the OTES observation between 6 μm and 50 μm, where the OTES noise equivalent spectral radiance (NESR, which represents the 1σ variation in calibrated radiance) is the lowest[15].

Next, for each OTES spot and for each observation time, we use the aforementioned lookup table of thermophysical simulations to train a neural network that generalizes the prediction of the radiance as a function of Γ and θ. The step of training the neural networks and using them in the fitting routine makes the exploration of the large, multi-dimensional parameter space of solutions computationally possible. This approach is particularly potent for the case of Bennu because day-side and night-side data are available, with a wide spectral wavelength range[15,17]. Seventy per cent of the model radiances are used for training via stochastic gradient descent and a neural network architecture with one hidden layer of ten neurons, which is the optimal scheme[17]. Another 15% of the dataset is used to protect the networks against overfitting the training data. We use the last 15% of the dataset to assess the networks' performance on unseen data in terms of mean squared error between the predicted and target radiances. The networks generalize well the prediction of the model radiances at testing: the average errors are equal to 0.2% and 0.9% of the radiance peak value for $\Gamma = 350$ J m^{-2} K^{-1} s$^{-0.5}$ and $\theta = 43°$ (the average surface thermophysical properties of Bennu[10]) for the 3:20 am and 3:00 pm observations, respectively; the correlation coefficient between predicted and target radiances is greater than 0.99.

Next, we use the networks to simulate the radiance L_{regolith} emitted by fine regolith of thermal inertia Γ_{P} and that emitted by rocks of thermal inertia Γ_{R} (L_{rock}), and linearly combine them to model the radiance L_{model} emitted by a mixture of fine regolith and rocks:

$$L_{\mathrm{model}}(f_{\mathrm{s}}, \theta, \Gamma_{\mathrm{P}}, \Gamma_{\mathrm{R}}, \alpha) = f_{\mathrm{s}}\left[\alpha L_{\mathrm{regolith}}(\Gamma_{\mathrm{P}}, \theta) + (1-\alpha) L_{\mathrm{rock}}(\Gamma_{\mathrm{R}}, \theta)\right], \quad (1)$$

where f_{s} is an optional scaling factor that is adjusted during the model fit to account for small modelling errors caused by (unknown) inaccuracies in the topographic model and/or potential deficiencies of the surface roughness[10]. Γ_{P} assumes values between 25 J m^{-2} K^{-1} s$^{-0.5}$ and Γ_{c}, and Γ_{R} between Γ_{c} and 2,500 J m^{-2} K^{-1} s$^{-0.5}$, where Γ_{c} is the thermal inertia cut-off value of regolith whose particles have $D_{\mathrm{P}} = l_{\mathrm{s}}$. It is computed as follows. For each area, we postulate that fine regolith is produced by the comminution of local rocks by meteoroid impacts[36] and thermal cracking[24]. This implies that fine regolith particles inherit the thermal conductivity κ, grain density ρ_{s} and porosity Φ of the rock. κ is obtained using the fit of meteorite values[37]:

$$\kappa(\Phi) = \frac{\Gamma_{\mathrm{R}}^2}{c_{\mathrm{P}}\rho_{\mathrm{s}}(1-\Phi)} = \frac{0.11(1-\Phi)}{\Phi}, \quad (2)$$

where $\rho_{\mathrm{s}} = 2{,}920$ kg m^{-3} for CM meteorites[38] and c_{P} is the heat capacity for the meteorite CM2 Cold Bokkeveld[20] at the OTES spot's mean diurnal temperature[10]. Although alternative relationships of thermal conductivity and rock porosity are available[19], equation (2) is the model that also fits well more recent results for super-weak CM-like materials[23]. Because Γ_{R} is a fitted parameter, the procedure for determining Γ_{c} is necessarily iterative; we initialize the iteration assuming Γ_{R} equal to the single-component thermal inertia derived by previous studies[10]. We use a standard[39] regolith model to calculate particulate regolith bulk thermal conductivity (κ_{P}) as a function of D_{P}. These values are compared to respective values of $l_{\mathrm{s}} = l_{\mathrm{s}}(\kappa_{\mathrm{P}})$ to find the value of κ_{P} where $D_{\mathrm{P}} = l_{\mathrm{s}}$. This value of κ_{P} is combined with c_{P} and $\rho = \rho_{\mathrm{s}}(1-\Phi)(1-\varphi)$ to calculate Γ_{c} (φ is the macroporosity of the regolith, that is, the volume of voids between particles). We use published[10] model parameters and assume $\zeta = 0.68 + 7.6 \times 10^{-5}/D_{\mathrm{P}}$ as the ratio of the effective distance of radiative heat transfer in the voids between particles to the geometric size of the voids[39,40], $\xi = 0.12$ as the degree of reduction of the thermal conductance at the contacts between particles owing to the microscopic surface roughness[39], $\varepsilon = 0.95$ as the infrared emissivity[10] and

$\varphi = 40\%$ as the regolith macroporosity. The last value is used often and represents a loose random packing of spherical particles[41]. We take into account thermal gradients within individual regolith particles using the non-isothermal correction factor[41], as in previous work[10].

For a given Γ_c and assuming θ from published[10] results, we explore all possible combinations of the free parameters $\mathbf{x} = (f_s^{3:00\text{pm}}, f_s^{3:20\text{am}}, \Gamma_P, \Gamma_R, \alpha)$ to identify the best-fitting radiance that minimizes the error function

$$\chi_r^2 = \frac{1}{\text{obs} - \text{df}} \left\{ \sum_{\lambda=6\,\mu\text{m}}^{50\,\mu\text{m}} \frac{\left[L_{\text{model}}^{3:00\text{pm}}(\mathbf{x}, \lambda) - L_{\text{OTES}}^{3:00\text{pm}}(\lambda)\right]^2}{\sigma^2} + \sum_{\lambda=6\,\mu\text{m}}^{50\,\mu\text{m}} \frac{\left[L_{\text{model}}^{3:20\text{pm}}(\mathbf{x}, \lambda) - L_{\text{OTES}}^{3:20\text{pm}}(\lambda)\right]^2}{\sigma^2} \right\},$$

where L_{OTES} is the observed radiance re-sampled with a step of 1 μm, σ is the error measurement, equal to three times the OTES' pre-flight[15] 772-Hz NESR, obs is the number of observations and df = 5 is the number of parameters to fit. The uncertainties of the free parameters are computed as the standard deviation of the set of solutions with $\chi_r^2 < \min(\chi_r^2) + [2/(\text{obs} - \text{df})]^{1/2}$, as typically done in thermophysical modelling[42]. On completion of the fitting, the best-fitting Γ_R is used to update the value of Γ_c, which is in turn used to re-compute the best-fitting $(f_s^{3:00\text{pm}}, f_s^{3:20\text{am}}, \Gamma_P, \Gamma_R, \alpha)$. This loop is repeated until $|\Gamma_R^i - \Gamma_R^{i-1}| < \sigma_R^{i-1}$, where i indicates the present iteration and σ_R^{i-1} is the standard deviation of Γ_R obtained at the $(i-1)$th iteration. Convergence is typically reached in four iterations. Once the analysis is completed, we add a cautionary 10% relative error to the uncertainties because previous studies[10] found that the thermophysical solution obtained by fitting the 3:00 pm and 3:20 am data are within 10% of the value obtained by including additional OTES data acquired at other times of day.

Finally, we reject 25 spots for which the best-fitting solutions have $\chi_r^2 > 10$ and/or for which no convergence is found for $\Gamma_R \leq 2{,}490$ J m^{-2} K^{-1} s$^{-0.5}$. We carry out the analysis and tests reported below on the remaining 97 spots (Supplementary Table 1).

Tests of the robustness of the results

We test whether the measured α values are consistent with the surface abundance of unresolved materials seen in PolyCam[33] images. We do this test for the spots 609505286:610098718 and 609504794:610100730 centred at Osprey and at Nightingale, for which rock mapping has been performed[43] down to $D_P = 2$ cm $\lesssim l_s$ (Extended Data Fig. 2). We note that the OTES spots have areas at least 38 and 20 times larger than those within which rocks were visually mapped at Osprey and Nightingale, respectively.

We also test whether α is always smaller than or equal to the surface area of unresolved materials that we can visually see, at coarser spatial resolution than at Osprey and at Nightingale, within the entire OTES spot. We choose the spots 609493058:610103962 and 609487186:610098206 and perform rock mapping similar to that done[43] on PolyCam images at a spatial resolution of 5 cm per pixel (greater than l_s). The area of each rock is computed as that of a circle with diameter equal to the rock's longest dimension. One minus the sum of the rocks' areas divided by the area of the OTES spot is provided as the percentage of unresolved material in Extended Data Fig. 3, along with the value of α. We also check that the size distributions of the mapped rocks are consistent with that globally mapped on Bennu[34], meaning that the two sites are representative of average Bennu.

We use a two-sided Spearman test to reject the null hypothesis that a random distribution of Γ_R and α values could produce the observed correlation in Fig. 1 (Extended Data Fig. 4). To take into account uncertainties in the values of Γ_R and α, we perform the Spearman test 10,000 times, in each trial varying Γ_R and α within their uncertainties. We draw the samples from Gaussian distributions with mean and standard deviation equal to the nominal value and uncertainties of Γ_R and α.

We repeat the Spearman test after we reject 13 areas where large dark boulders fill the OTES spot (red data points in Fig. 1). Bennu's dark boulders tend to have low Γ_R values[10,34], although the lower limit of Γ_R is unknown because only one boulder was spatially resolved by the OTES instrument[10]. If $\Gamma_R < \Gamma_c$ for the boulders, then their surface abundance would erroneously contribute to the surface abundance of fine regolith (α) instead of them being counted as rocks, with the caveat that fine regolith could be present on top of the boulders[10].

We investigate whether the Γ_R–α correlation is sensitive to the assumed regolith macroporosity φ (Extended Data Fig. 5). We repeat the thermophysical modelling of all OTES spots for a low-end value of $\varphi = 15\%$, which is an estimate for the whole asteroid based on a boulder size–frequency distribution analysis[44], and a high-end value of $\varphi = 60\%$, which is a compromise reduction from much higher values used in previous studies (for example, $\varphi = 80\%$[45], which we consider unlikely for a polydisperse size–frequency distribution). We perform a 3σ test on the solutions to identify the areas where $(\Gamma_P, \Gamma_R, \alpha)$ for $\varphi = 15\%$ and for $\varphi = 60\%$ are statistically distinct from those for $\varphi = 40\%$. This test is done considering only the spots where a converged solution is found for both macroporosities: 93 spots for $\varphi = 40\%$ versus $\varphi = 15\%$ and 90 spots for $\varphi = 40\%$ versus $\varphi = 60\%$. We repeat the Spearman test to assess the robustness of the correlation against removing the areas with statistically distinct solutions from the dataset.

We investigate whether the Γ_R–α correlation is an artefact due to the assumption of linear mixing between the radiances emitted by fine regolith and rocks (equation (1)). We simulate synthetic radiances emitted from a single triangular facet with zero roughness and thermal inertia values following the step function

$$\alpha(\Gamma) = \begin{cases} 100\%, & \text{for } \Gamma \leq \Gamma_c = 100\ \text{J m}^{-2}\,\text{K}^{-1}\text{s}^{-0.5}, \\ 0\%, & \text{for } 100\ \text{J m}^{-2}\,\text{K}^{-1}\text{s}^{-0.5} < \Gamma < 2{,}500\ \text{J m}^{-2}\text{K}^{-1}\text{s}^{-0.5}. \end{cases} \quad (3)$$

We simulate the observation of these model radiances by OTES and fit them using our thermophysical model to see whether we retrieve the modelled step function (equation (3)) or a correlation similar to that in Fig. 1 is instead obtained (Extended Data Fig. 6).

Finally, it has been suggested[10,34,46] that dark boulders (normal reflectance, 0.034–0.049) are more abundant, can have larger diameters and have lower thermal inertia than bright boulders (normal reflectance, 0.049–0.074). These boulder properties could mimic the Γ_R–α correlation in Fig. 1 if α were negatively correlated with the area of the largest boulder in the OTES spot. Using a boulder database[46], we plot α as a function of the size of the largest boulder and perform the Spearman test to investigate whether these quantities are correlated (Extended Data Fig. 7).

Interpretation of the results

For each OTES spot, we compute the rock porosity Φ from the best-fitting Γ_R using equation (2), assuming ρ_s and c_P as for the computation of Γ_c. The range of Φ for Ryugu in Fig. 2 corresponds to that estimated[19] using equation (2) for the boulder observed by the MASCOT infrared radiometer, a typical[25] type of boulder on Ryugu. We also use equation (2) to compute Φ for the rocks on Itokawa from the published[17] value of $\Gamma_R = 894 \pm 122$ J m^{-2} K^{-1} s$^{-0.5}$ assuming the composition of LL chondrites, which is the same as that of the samples returned from Itokawa[47]: $\rho_s = 3{,}220$ kg m^{-3} and $c_P = 682$ J kg^{-1} K^{-1}. We compute the uncertainty of Itokawa's Φ as $\sigma(\Phi) = \partial\Phi/\partial\Gamma_R \times \sigma(\Gamma_R)$, where $\sigma(\Gamma_R)$ is the uncertainty of Itokawa's Γ_R from ref. [17].

Next, we use this information to estimate the time t_B to break a rock of diameter D_R by thermal fatigue. We use known models[24,48] to simulate a bed of polydispersed spherical rocks, the surface of which is exposed to cyclic temperature variations driven by sunlight. On each rock, an initially submillimetre-sized fracture placed on the surface propagates downwards in the rock (towards the centre of the asteroid) until its size a

becomes equal to D_R, which is the condition for rock break-up. The time to fracture t_B may be calculated from the fracture growth rate da/dN, which is typically approximated[24] using Paris' law: $da/dN = C[\Delta K_I(a)]^n$, where N is the number of temperature cycles, C and n are the Paris' law pre-factor and exponent and have values determined from experiments or analogy with asteroid simulant materials[24], and ΔK_I is the maximum variation of the stress intensity factor K_I for fracture-opening mode. ΔK_I is related to the stress τ experienced by the material during a temperature cycle: $\Delta K_I \propto \tau \propto \Delta T$, where ΔT is the maximum diurnal temperature excursion[24]. Moreover, from equation (23) of ref. [48] we can write $t_B/p = \Lambda'(D_R/l_s)^{1/m}$, where Λ' is a scaling parameter defined as in ref. [48] and

$$m = \begin{cases} 1/(1-n) & \text{for } D_R/l_s \leq 1, \\ 1/(n-1) & \text{for } D_R/l_s > 1. \end{cases}$$

Hence

$$\frac{t_B}{p} = N = \Lambda'' \left(\frac{D_R}{l_s}\right)^{\frac{1}{m}} (\Delta T)^{-n} \tag{4}$$

Given N cycles are required to break a rock with a certain D_R/l_s, material properties, geometry and ΔT, we derive the value of the scaling parameter Λ'' and use equation (4) to predict t_B for rocks of different sizes at different ΔT. First, we calculate l_s to be 6.4 cm and 8.6 cm for the carbonaceous and the ordinary chondrite of ref. [24]. At $D_R = l_s$, figure 1 in ref. [24] then gives $t_B = 3.5 \times 10^3$ years and 6.3×10^3 years, respectively, corresponding to $N = 1.4 \times 10^6$ and $N = 14 \times 10^6$ cycles, given $p = 6$ h. We take ΔT from extended data figure 2 in ref. [24]. Next, we use equation (4) to derive t_B as a function of D_R for values of l_s, p and ΔT that are more appropriate for Bennu, Ryugu and Itokawa than those in ref. [24]. We take the carbonaceous chondrite properties from ref. [24], but use $\Gamma_R = 500$ J m^{-2} K^{-1} s$^{-0.5}$, which is more appropriate for the high-Φ, low-Γ_R rocks that dominate Bennu's (Fig. 2) and Ryugu's[18,19,25] surfaces. For the ordinary chondrite, we use $\Gamma_R = 900$ J m^{-2} K^{-1} s$^{-0.5}$, as was derived from astronomical observations[17] of Itokawa, and assume that this parameter could also represent low-Φ, high-Γ_R rocks that may be present on Bennu's and Ryugu's surface, but in lower abundance than the high-Φ, low-Γ_R rocks. The rotation periods are $p = 4.296$ h, 7.63 h and 12.1 h for Bennu[49], Ryugu[50] and Itokawa[51], respectively. However, because these rotation periods could have been different[49] in the past, owing to the Yarkovsky–O'Keefe–Radzievskii–Paddack (YORP) effect, we consider generic low-Γ_R, high-Φ and high-Γ_R, low-Φ cases with $p = 4.296$ h and 12.1 h for a total of four cases. For each of these cases, we calculate l_s and run a thermophysical model to determine, at a heliocentric distance of 1.2 AU, ΔT. Finally, using equation (4), we produce Extended Data Fig. 8.

Data availability

Raw through-calibrated OTES[52] and OCAMS[53] data are available via the Planetary Data System (https://sbn.psi.edu/pds/resource/orex/). The SPC/OLA v34 shape model is available via the Small Body Mapping Tool (http://sbmt.jhuapl.edu/). The IDs of the OTES observations used here and the best-fitting solutions for the thermophysical model are provided in Supplementary Table 1. The boulder size, location and reflectance used to test the robustness of the results are available in refs. [34,46]. Source data are provided with this paper.

Code availability

The thermophysical analysis reported here uses custom code based on the thermophysical model of ref. [16], available at https://www.oca.eu/images/LAGRANGE/pages_perso/delbo/thermops.tar.gz. The code to compute the geometry of the OTES acquisitions and boresight is available at https://doi.org/10.5281/zenodo.4781752 (ref. [54]). The code to compute Γ_c for the thermophysical analysis is available at https://doi.org/10.5281/zenodo.4763783 (ref. [55]). The rock mapping in Extended Data Fig. 3 was performed using the SAOImageDS9 software available at https://sites.google.com/cfa.harvard.edu/saoimageds9. Other codes that support the findings of this study are available at https://doi.org/10.5281/zenodo.4771035 (ref. [56]).

32. Bennett, C. et al. A high-resolution global basemap of (101955) Bennu. *Icarus* **357**, 113690 (2021).
33. Rizk, B. et al. OCAMS: the OSIRIS-REx camera suite. *Space Sci. Rev.* **214**, 26 (2018).
34. DellaGiustina, D. et al. Properties of rubble-pile asteroid (101955) Bennu from OSIRIS-REx imaging and thermal analysis. *Nat. Astron.* **3**, 341–351 (2019).
35. Barnouin, O. et al. Digital terrain mapping by the OSIRIS-REx mission. *Planet. Space Sci.* **180**, 104764 (2020).
36. Horz, F. & Cintala, M. Impact experiments related to the evolution of planetary regoliths. *Meteorit. Planet. Sci.* **31** (Suppl.), A65 (1996).
37. Flynn, G. J., Consolmagno, G. J., Brown, P. & Macke, R. J. Physical properties of the stone meteorites: implications for the properties of their parent bodies. *Chem. Erde* **78**, 269–298 (2018).
38. Macke, R. J., Consolmagno, G. J. & Britt, D. T. Density, porosity, and magnetic susceptibility of carbonaceous chondrites. *Meteorit. Planet. Sci.* **46**, 1842–1862 (2011).
39. Sakatani, N., Ogawa, K., Arakawa, M. & Tanaka, S. Thermal conductivity of lunar regolith simulant JSC-1A under vacuum. *Icarus* **309**, 13–24 (2018).
40. Wada, K. et al. Asteroid Ryugu before the Hayabusa2 encounter. *Prog. Earth Planet. Sci.* **5**, 82 (2018).
41. Ryan, A. J., Pino Muñoz, D., Bernacki, M. & Delbo, M. Full-field modeling of heat transfer in asteroid regolith: radiative thermal conductivity of polydisperse particulates. *J. Geophys. Ress Planets* **125**, e2019JE006100 (2020).
42. Hanuš, J., Delbo, M., Ďurech, J. & Ali-Lagoa, V. Thermophysical modeling of main-belt asteroids from WISE thermal data. *Icarus* **309**, 297–337 (2018).
43. Burke, K. N. et al. Particle size-frequency distributions of the OSIRIS-REx candidate sample sites on asteroid (101955) Bennu. *Remote Sens.* **13**, 1315 (2021).
44. Biele, J. et al. Macroporosity and grain density of rubble pile asteroid (101955) Bennu. In *AGU Fall Meeting 2020* Vol. 1, P037–04 (2020).
45. Gundlach, B. & Blum, J. A new method to determine the grain size of planetary regolith. *Icarus* **223**, 479–492 (2013).
46. DellaGiustina, D. N. et al. Variations in color and reflectance on the surface of asteroid (101955) Bennu. *Science* **370**, eabc3660 (2020).
47. Nakamura, T. et al. Itokawa dust particles: a direct link between S-type asteroids and ordinary chondrites. *Science* **333**, 1113–1116 (2011).
48. El Mir, C., Ramesh, K. T. & Delbo, M. The efficiency of thermal fatigue in regolith generation on small airless bodies. *Icarus* **333**, 356–370 (2019).
49. Hergenrother, C. W. et al. The operational environment and rotational acceleration of asteroid (101955) Bennu from OSIRIS-REx observations. *Nat. Commun.* **10**, 1291 (2019).
50. Watanabe, S. et al. Hayabusa2 arrives at the carbonaceous asteroid 162173 Ryugu—a spinning top-shaped rubble pile. *Science* **364**, 268–272 (2019).
51. Demura, H. et al. Pole and global shape of 25143 Itokawa. *Science* **312**, 1347–1349 (2006).
52. Christensen, P., Hamilton, V., Anwar, S., Mehall, G. & Lauretta, D. *OSIRIS-REx Thermal Emission Spectrometer Bundle* urn:nasa:pds:orex.otes, https://sbn.psi.edu/pds/resource/orex/ (NASA Planetary Data System, 2019).
53. Rizk, B., Golish, D., DellaGiustina, D. & Lauretta, D. *OSIRIS-REx Camera Suite Bundle* urn:nasa:pds:orex.ocams, https://sbn.psi.edu/pds/resource/orex/ (NASA Planetary Data System, 2019).
54. Deshapriya, J. D. P. *OTES geoWriter* https://doi.org/10.5281/zenodo.4781752 (2021).
55. Ryan, A. *Regolith Heat Transfer Code for Manuscript "Rock Porosity Drives Regolith Buildup on Carbon-Rich Versus Stony Asteroids"* https://doi.org/10.5281/zenodo.4763783 (2021).
56. Cambioni, S., Delbo, M. & Poggiali, G. *Codes for Two-Component Thermophysical Analysis of Asteroid (101955) Bennu* https://doi.org/10.5281/zenodo.4771035 (2021).

Acknowledgements This material is based on work supported by NASA under contract NNM10AA11C issued through the New Frontiers Program. We are grateful to the entire OSIRIS-REx team for making the encounter with Bennu possible, to C. Wolner and F. Murphy for editorial help, and to the OPAL infrastructure of the Observatoire de la Côte d'Azur (CRIMSON) for providing computational resources and support. S.C. thanks the University of Arizona for supporting this study. M.D., C.A., J.D.P.D. and M.A.B. acknowledge the French space agency CNES. C.A. and M.D. acknowledge support from ANR "ORIGINS" (ANR-18-CE31-0014). C.A. was supported by the French National Research Agency under the project "Investissements d'Avenir" UCAJEDI ANR-15-IDEX-01. G.P. and J.R.B. were supported by Italian Space Agency grant agreement INAF/ASI number 2017-37-H.O. B.R. acknowledges financial support from the UK Science and Technology Facilities Council (STFC). E.C. thanks CSA, NSERC, CFI, MRIF and UWinnipeg for supporting this study.

Author contributions S.C. led the project, the interpretation of the results and the manuscript development, and performed the thermophysical simulations and data analysis. M.D. provided the thermophysical software, performed the thermal cracking calculations, and contributed to the interpretation of the results and the development of the manuscript. G.P. developed the pipeline to retrieve OTES detailed survey data and performed rock mapping in PolyCam images. C.A. curated the discussion on meteoroid bombardment and contributed to writing the manuscript. A.J.R. contributed with the code to convert thermal inertia values in fine-regolith particle size and developed the iterative approach to determine the cut-off value of thermal inertia, together with S.C. J.D.P.D. extracted the observation geometry of the spacecraft and Bennu from mission kernels. R.-L.B. proposed important tests of the robustness of the results. E.A., W.F.B. and J.R.B. contributed to the interpretation of the data and writing of the manuscript. D.N.D., K.N.B., C.A.B. and K.J.W. provided support in the interpretation of spacecraft imagery. J.P.E. and B.R. contributed to the data interpretation during the OSIRIS-REx Thermal Analysis Working Group meetings, and to the design of the observations and data acquisition. M.A.B. and E.C. contributed to the interpretation of the results. D.S.L. made this study possible as the PI of the OSIRIS-REx mission and contributed to the discussion of the results.

Competing interests The authors declare no competing interests.

Additional information

Supplementary information The online version contains supplementary material available at https://doi.org/10.1038/s41586-021-03816-5.

Correspondence and requests for materials should be addressed to S. Cambioni.

Peer review information *Nature* thanks Guy Consolmagno and Seiji Sugita for their contribution to the peer review of this work. Peer reviewer reports are available.

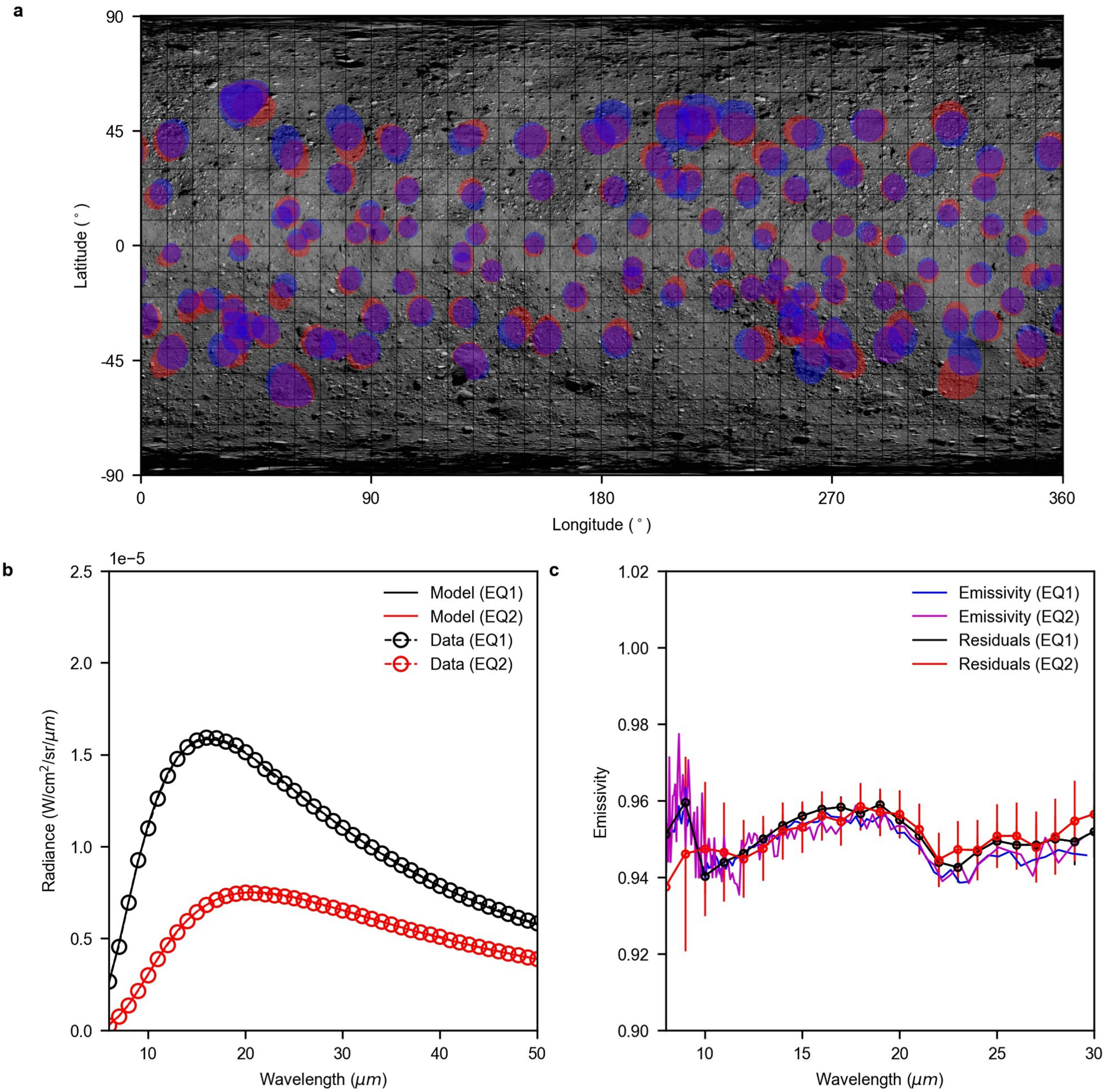

Extended Data Fig. 1 | The thermal inertia of Bennu's rocks and the surface abundance of fine regolith were measured in 122 quasi-randomly–distributed regions. a, OTES spots on Bennu plotted on the global basemap of Bennu[32] as function of longitude and latitude (red: Equatorial Station 1 at 3:00 pm, or EQ1; blue: Equatorial Station 2 at 3:20 am, or EQ2). **b**, comparison between modelled and observed radiance for one of the 122 areas (ID: 609491396:610102222). **c**, comparison between the emissivity of Bennu and the residuals of the analysis for the spots 609491396:610102222; the residual curves closely resemble Bennu's emissivity, which is not modelled by our thermophysical model. The error bars correspond to 3 times the Noise Equivalent Spectral Radiance of the OTES instrument[15]. Credit for global mosaic in panel a: NASA/Goddard/University of Arizona.

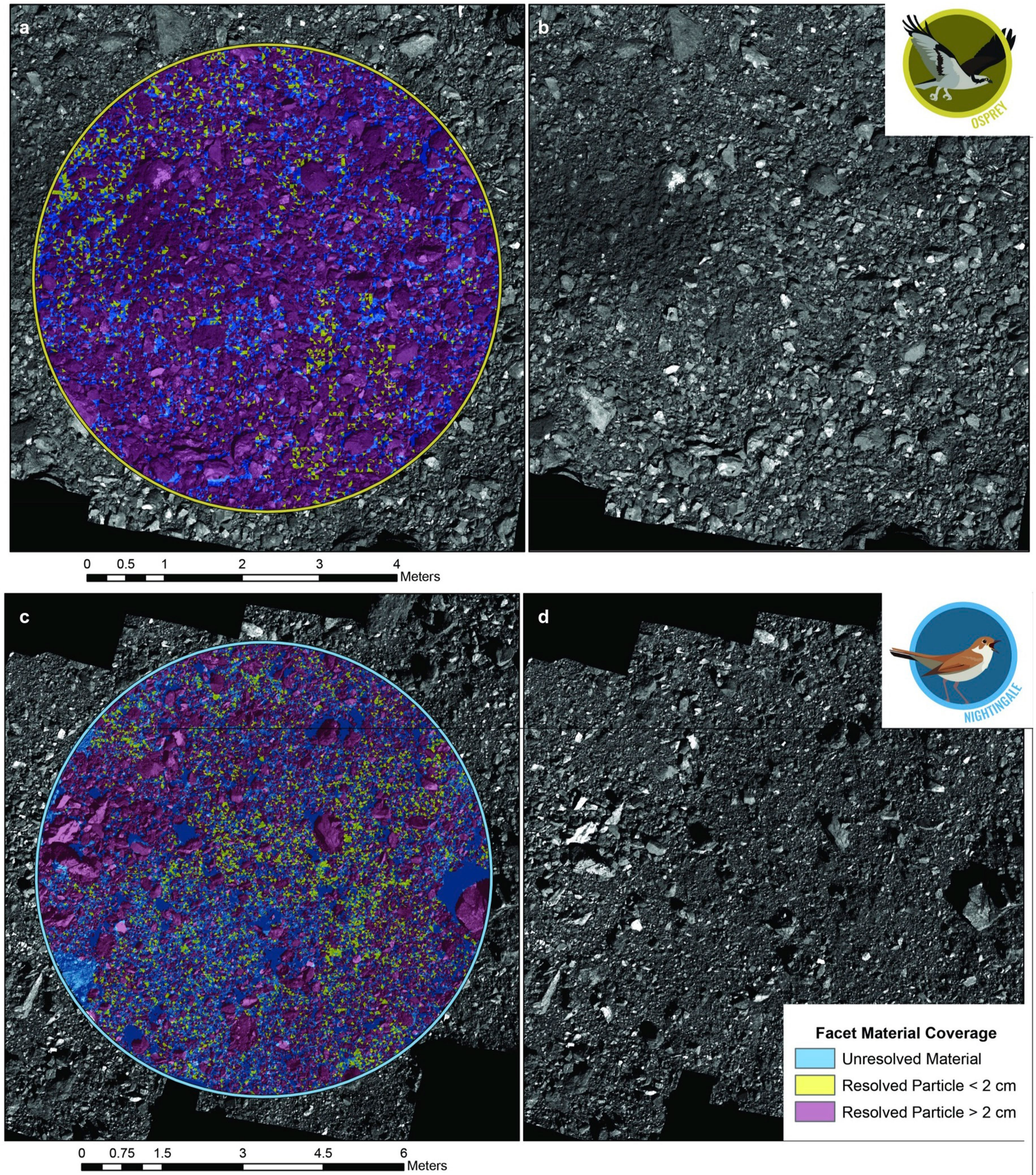

Extended Data Fig. 2 | There is less fine regolith at the OSIRIS-REx's backup sampling site Osprey than at the primary sampling site Nightingale. Blue and yellow pixels represent areas where no particles bigger than 2 cm, ~l_s, were mapped by ref. [43]. The value $D_P \approx l_s$ is the upper limit for the sizes of fine regolith detected by our thermophysical model. There are fewer blue and yellow pixels at Osprey (image resolution: 0.3 cm per pixel, panels **a**, **b**) than at Nightingale (image resolution: 0.4 cm per pixel, panels **c**, **d**), implying that Osprey has less unresolved material than Nightingale. Consistently and independently, our thermophysical model indicates $\alpha_{\mathrm{Osprey}} < \alpha_{\mathrm{Nightingale}}$ (Supplementary Table 1, spots 609505286:610098718 and 609504794:610100730, respectively). Credit for bird graphics and PolyCam images: NASA/Goddard/University of Arizona.

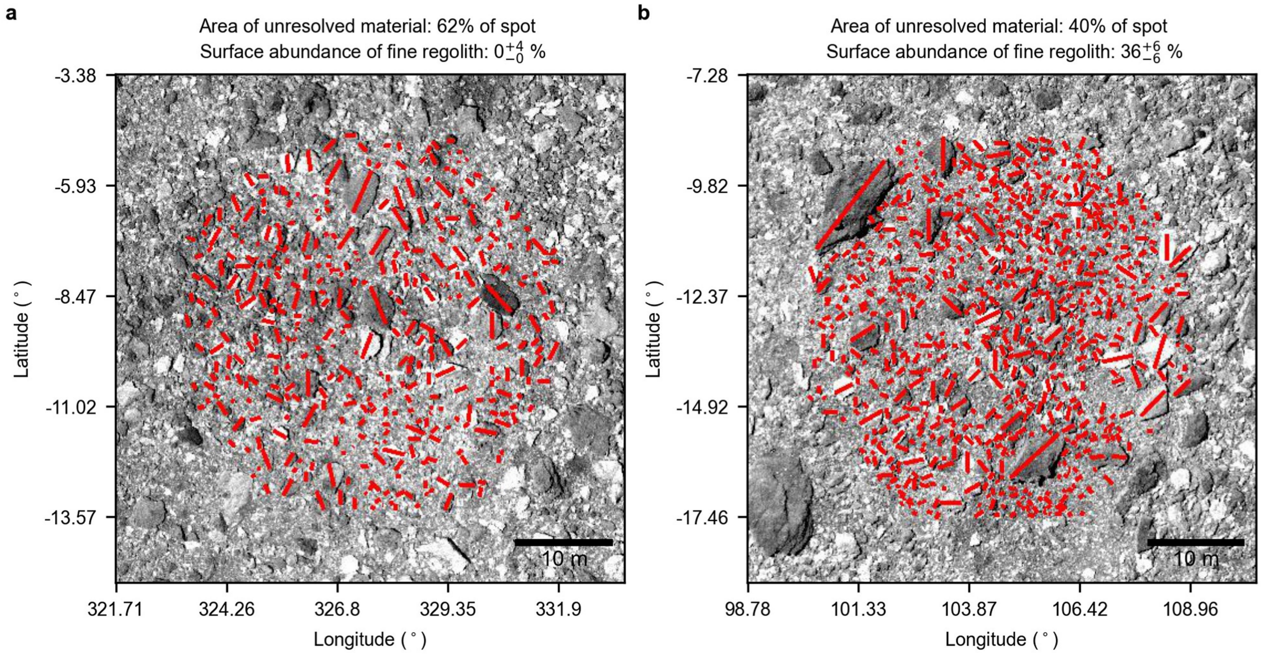

Extended Data Fig. 3 | The fine-regolith abundance derived from OTES data is lower than the area of unresolved material measured in Bennu's images. Our visual mapping and size measurement of rocks within two OTES spots: **a**, OTES spots 609493058:610103962; **b**, OTES spots 609487186:610098206. In both areas, the values of α from our thermophysical solution are smaller than the areas of unresolved materials seen in the images. Given the coarse PolyCam[32] resolution, it is possible that there are unmapped particles larger than l_s (but smaller than the image resolution) that our thermophysical model detects as rocks and thus do not contribute to the value of α. Credit for PolyCam images: NASA/Goddard/University of Arizona.

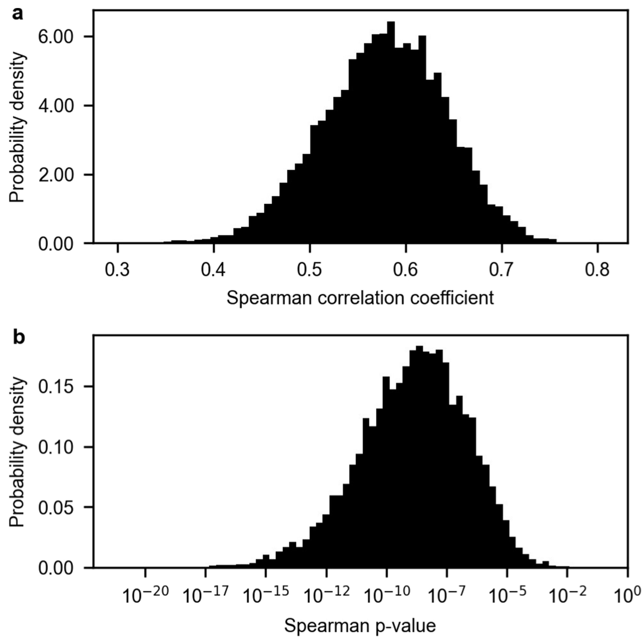

Extended Data Fig. 4 | The correlation between Γ_R and α is statistically significant. **a**, Spearman correlation coefficient. **b**, Spearman *P*-value; a Spearman $P < 0.05$ indicates that the correlation between Γ_R and α is statistically significant. The figure corresponds to the results for a value of regolith macroporosity of $\varphi = 40\%$.

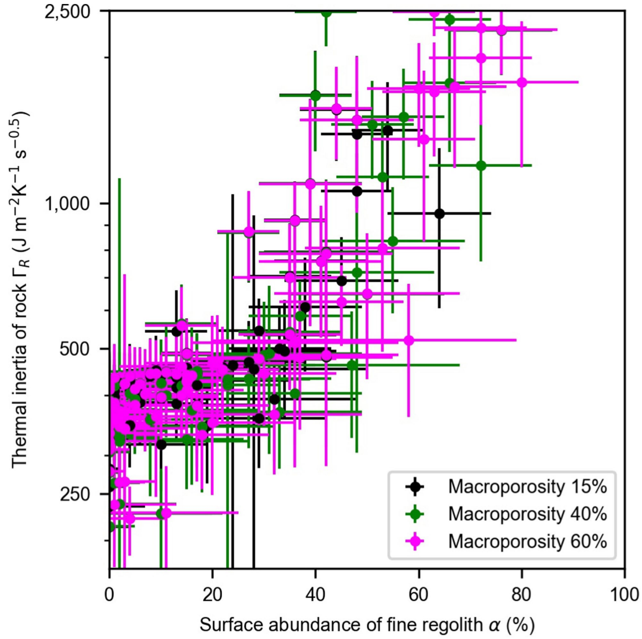

Extended Data Fig. 5 | The correlation between Γ_R and α is robust against the choice of the fine-regolith macroporosity. The results for macroporosity $\varphi = 15\%$ and $\varphi = 60\%$ have Spearman correlation coefficients 0.56 ± 0.06 and 0.58 ± 0.06, probability of non-correlation $P < 0.05$, and are within 3 standard deviations of the best-fit values for regolith macroporosity of $\varphi = 40\%$ in 99% and 92% of the cases, respectively. The correlations are robust against removing the areas whose solutions are statistically distinct from the data set with macroporosity $\varphi = 40\%$ (Spearman correlation index: 0.55 ± 0.07 and $P < 0.05$ in 100% of 10,000 trials). The error bars correspond to 1 standard deviation (Supplementary Table 1; Methods) computed on ~450 and ~880 samples on average. The results for a regolith macroporosity of $\varphi = 40\%$ are described in the main text (Fig. 1).

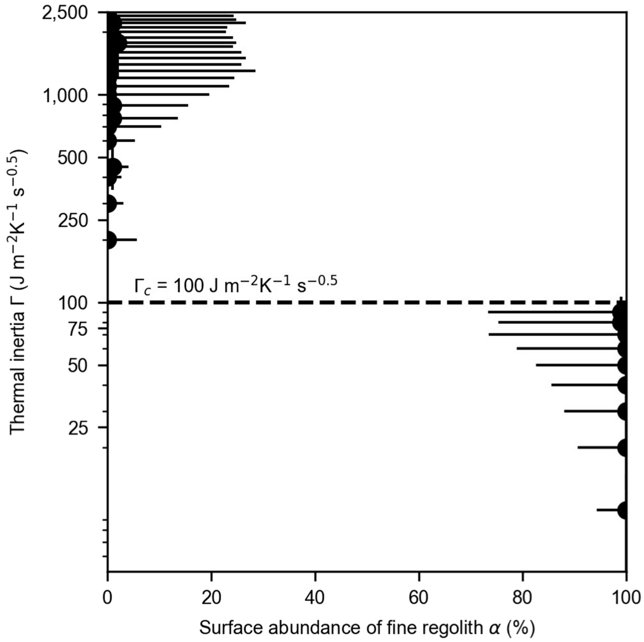

Extended Data Fig. 6 | The correlation between Γ_R and α is not an artefact of thermophysical modelling. We fit model radiances emitted by a single triangular facet with zero roughness; if the thermal inertia $\Gamma \le \Gamma_c = 100\,\mathrm{J\,m^{-2}K^{-1}s^{-0.5}}$, then $\alpha = 100\%$, and if $\Gamma_c < \Gamma < 2{,}500\,\mathrm{J\,m^{-2}K^{-1}s^{-0.5}}$, then $\alpha = 0\%$. We retrieve the expected step function of α as a function of Γ, indicating that the correlation in Fig. 1 is unlikely to be an artefact of the model. The error bars correspond to 1 standard deviation computed on ~1.76×10^4 samples on average (Methods).

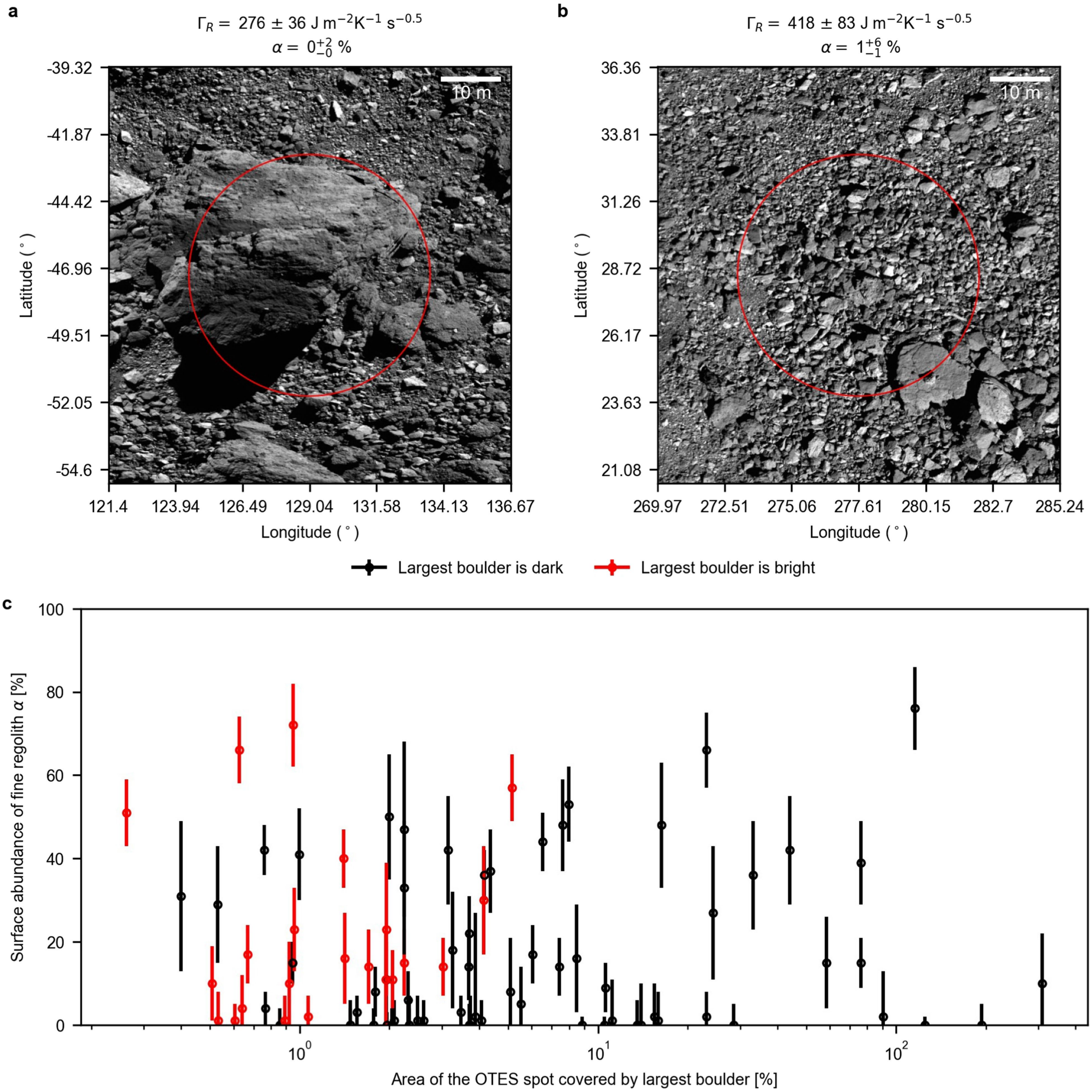

Extended Data Fig. 7 | The correlation between Γ_R and α is not a geometric effect due to boulders' sizes. a, PolyCam image of the surface corresponding to spots 609486110:610097198 where α is low probably because the spots are filled by a large, dark boulder. **b**, PolyCam image of the surface corresponding to spots 609495164:610106090 where α does not correlate with the size of the largest boulder; this is representative of most of the surveyed areas. **c**, plot of α as function of the percentage of the OTES spot covered by the largest boulder on the surface. The Spearman test reveals that these two quantities have a probability of non-correlation above the critical threshold of 0.05 in 99.99% of 10,000 trials. This indicates that the Γ_R-α correlation of Fig. 1 is not the result of geometric effects. The error bars in panel c correspond to 1 standard deviation (Supplementary Table 1; Methods) computed on ~ 670 samples on average. Credit for global mosaic: NASA/Goddard/University of Arizona.

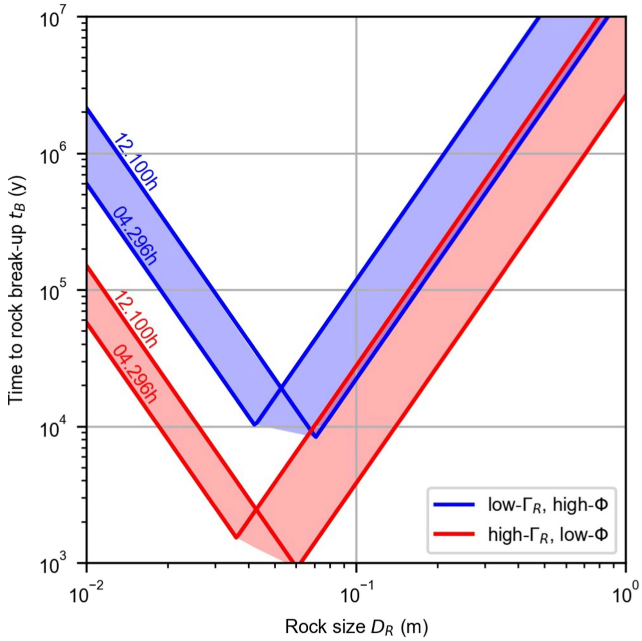

Extended Data Fig. 8 | The time required to thermally break rocks is shorter for low-porosity rocks than for high-porosity rocks. We consider the asteroid to be in near-Earth space and explore a range of rotation periods corresponding to the shaded areas. The latter is to take into account changes in the current rotation periods (4.296 h and 12.1 h for Bennu and Itokawa, respectively) that these asteroids may have experienced in the past[49] due to the Yarkovsky–O'Keefe–Radzievskii–Paddack (YORP) effect. We estimate that in their main belt source region, at about 2.3 au from the Sun, the time to break is ~60 times longer.

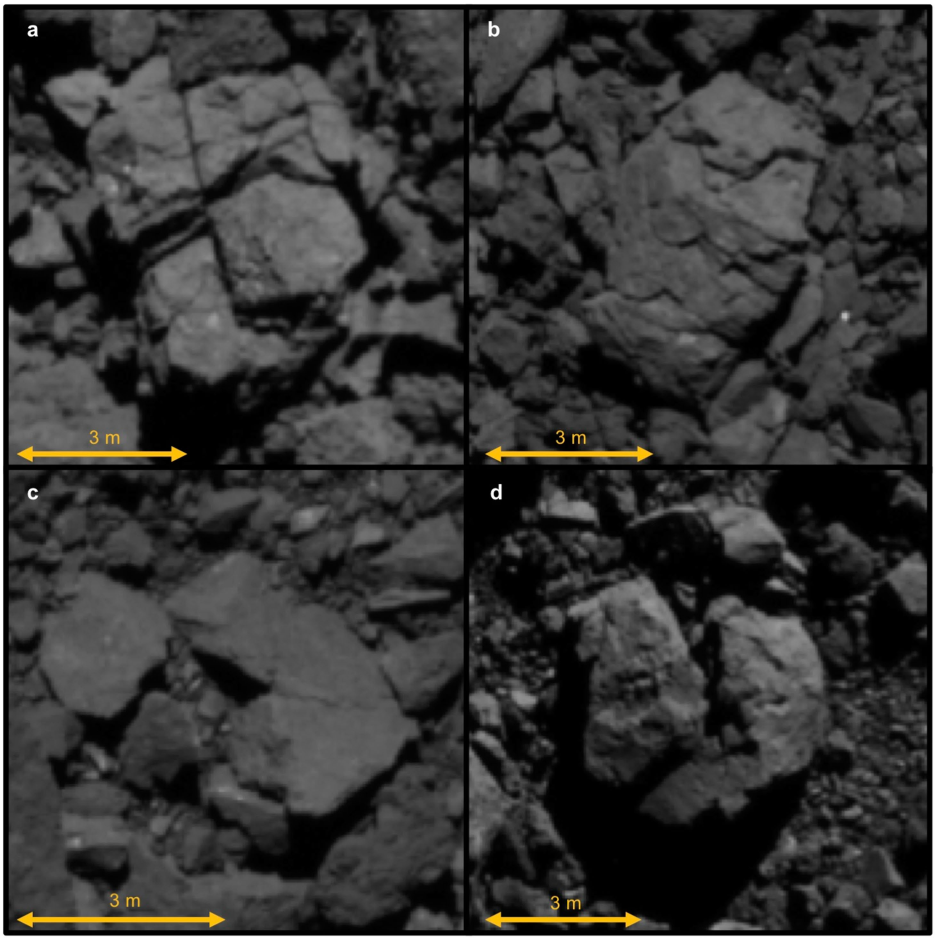

Extended Data Fig. 9 | Examples of in-situ boulder fragmentation on Bennu. **a**, a 5.4 m-diameter boulder located at 22° N 157° E. **b**, a 5.6 m-diameter boulder located at 42° N 170° E. **c**, a 5.3 m-diameter boulder located at 57° N 304° E. **d**, a 5 m-diameter boulder located at 39° S 203° E. The images are from the global mosaic[32] acquired by the PolyCam[33] imager of OCAMS. Credit for PolyCam images: NASA/Goddard/University of Arizona.